The Astrophysical Journal Letters, 951:L5 (11pp), 2023 July 1 https://doi.org/10.3847/2041-8213/acc9c8

A SPectroscopic Survey of Biased Halos in the Reionization Era (ASPIRE): A First Look at the Rest-frame Optical Spectra of $z > 6.5$ Quasars Using JWST

Jinyi Yang[1,39], Feige Wang[1], Xiaohui Fan[1], Joseph F. Hennawi[2,3], Aaron J. Barth[4], Eduardo Bañados[5], Fengwu Sun[1], Weizhe Liu[1], Zheng Cai[6], Linhua Jiang[7,8], Zihao Li[6], Masafusa Onoue[8,9], Jan-Torge Schindler[3], Yue Shen[10,11], Yunjing Wu[1,6], Aklant K. Bhowmick[12], Rebekka Bieri[13], Laura Blecha[14], Sarah Bosman[5], Jaclyn B. Champagne[1], Luis Colina[15,16], Thomas Connor[17,18], Tiago Costa[19], Frederick B. Davies[5], Roberto Decarli[20], Gisella De Rosa[21], Alyssa B. Drake[22], Eiichi Egami[1], Anna-Christina Eilers[23,40], Analis E. Evans[12], Emanuele Paolo Farina[24], Melanie Habouzit[5,25], Zoltan Haiman[26,27], Xiangyu Jin[1], Hyunsung D. Jun[28], Koki Kakiichi[29], Yana Khusanova[5], Girish Kulkarni[30], Federica Loiacono[20], Alessandro Lupi[31], Chiara Mazzucchelli[32], Zhiwei Pan[7,8], Sofía Rojas-Ruiz[5,41], Michael A. Strauss[33], Wei Leong Tee[1], Benny Trakhtenbrot[34], Maxime Trebitsch[35], Bram Venemans[3], Marianne Vestergaard[1,36], Marta Volonteri[37], Fabian Walter[5], Zhang-Liang Xie[5], Minghao Yue[1,23], Haowen Zhang[1], Huanian Zhang[38], and Siwei Zou[6]
[1] Steward Observatory, University of Arizona, 933 N Cherry Avenue, Tucson, AZ 85721, USA; jinyiyang@email.arizona.edu
[2] Department of Physics, University of California, Santa Barbara, CA 93106-9530, USA
[3] Leiden Observatory, Leiden University, Niels Bohrweg 2, NL-2333 CA Leiden, Netherlands
[4] Department of Physics and Astronomy, University of California, Irvine, CA 92697, USA
[5] Max Planck Institut für Astronomie, Königstuhl 17, D-69117, Heidelberg, Germany
[6] Department of Astronomy, Tsinghua University, Beijing 100084, People's Republic of China
[7] Department of Astronomy, School of Physics, Peking University, Beijing 100871, People's Republic of China
[8] Kavli Institute for Astronomy and Astrophysics, Peking University, Beijing 100871, People's Republic of China
[9] Kavli Institute for the Physics and Mathematics of the Universe (Kavli IPMU, WPI), The University of Tokyo, Chiba 277-8583, Japan
[10] Department of Astronomy, University of Illinois at Urbana-Champaign, Urbana, IL 61801, USA
[11] National Center for Supercomputing Applications, University of Illinois at Urbana-Champaign, Urbana, IL 61801, USA
[12] Department of Physics, University of Florida, Gainesville, FL 32611, USA
[13] Center for Space and Habitability, University of Bern, Gesellschaftsstrasse 6 (G6), Bern, Switzerland
[14] Department of Physics, University of Florida, Gainesville, FL 32611-8440, USA
[15] Centro de Astrobiología (CAB), CSIC-INTA, Ctra. de Ajalvir km 4, Torrejón de Ardoz, E-28850, Madrid, Spain
[16] International Associate, Cosmic Dawn Center (DAWN), Denmark
[17] Center for Astrophysics, Harvard & Smithsonian, 60 Garden Street, Cambridge, MA 02138, USA
[18] Jet Propulsion Laboratory, California Institute of Technology, 4800 Oak Grove Drive, Pasadena, CA 91109, USA
[19] Max-Planck-Institut für Astrophysik, Karl-Schwarzschild-Straße 1, D-85748 Garching b. München, Germany
[20] INAF—Osservatorio di Astrofisica e Scienza dello Spazio, via Gobetti 93/3, I-40129, Bologna, Italy
[21] Space Telescope Science Institute, 3700 San Martin Drive, Baltimore, MD 21210, USA
[22] Centre for Astrophysics Research, Department of Physics, Astronomy and Mathematics, University of Hertfordshire, Hatfield AL10 9AB, UK
[23] MIT Kavli Institute for Astrophysics and Space Research, 77 Massachusetts Avenue, Cambridge, MA 02139, USA
[24] Gemini Observatory, NSF's NOIRLab, 670 N A'ohoku Place, Hilo, HI 96720, USA
[25] Zentrum für Astronomie der Universität Heidelberg, ITA, Albert-Ueberle-Str. 2, D-69120 Heidelberg, Germany
[26] Department of Astronomy, Columbia University, New York, NY 10027, USA
[27] Department of Physics, Columbia University, New York, NY 10027, USA
[28] SNU Astronomy Research Center, Seoul National University, 1 Gwanak-ro, Gwanak-gu, Seoul 08826, Republic of Korea
[29] Department of Physics, Broida Hall, University of California, Santa Barbara, CA 93106-9530, USA
[30] Tata Institute of Fundamental Research, Homi Bhabha Road, Mumbai 400005, India
[31] Dipartimento di Fisica "G. Occhialini," Università degli Studi di Milano-Bicocca, Piazza della Scienza 3, I-20126 Milano, Italy
[32] Instituto de Estudios Astrofísicos, Facultad de Ingeniería y Ciencias, Universidad Diego Portales, Avenida Ejercito Libertador 441, Santiago, Chile
[33] Department of Astrophysical Sciences, Princeton University, Princeton, NJ 08544, USA
[34] School of Physics and Astronomy, Tel Aviv University, Tel Aviv 69978, Israel
[35] Kapteyn Astronomical Institute, University of Groningen, P.O. Box 800, 9700 AV Groningen, The Netherlands
[36] The Niels Bohr Institute, University of Copenhagen, Denmark
[37] Institut d'Astrophysique de Paris, Sorbonne Université, CNRS, UMR 7095, 98 bis bd Arago, F-75014 Paris, France
[38] Department of Astronomy, Huazhong University of Science and Technology, Wuhan, 430074, People's Republic of China
Received 2023 February 20; revised 2023 March 27; accepted 2023 March 30; published 2023 June 29

Abstract

Studies of rest-frame optical emission in quasars at $z > 6$ have historically been limited by the wavelengths accessible by ground-based telescopes. The James Webb Space Telescope (JWST) now offers the opportunity to

[39] Strittmatter Fellow.
[40] Pappalardo Fellow.
[41] Fellow of the International Max Planck Research School for Astronomy and Cosmic Physics at the University of Heidelberg (IMPRS-HD).

probe this emission deep into the reionization epoch. We report the observations of eight quasars at $z > 6.5$ using the JWST/NIRCam Wide Field Slitless Spectroscopy as a part of the "A SPectroscopic survey of biased halos In the Reionization Era (ASPIRE)" program. Our JWST spectra cover the quasars' emission between rest frame ~4100 and 5100 Å. The profiles of these quasars' broad Hβ emission lines span a full width at half maximum from 3000 to 6000 km s^{-1}. The Hβ-based virial black hole (BH) masses, ranging from 0.6 to 2.1 billion solar masses, are generally consistent with their Mg II-based BH masses. The new measurements based on the more reliable Hβ tracer thus confirm the existence of a billion solar-mass BHs in the reionization epoch. In the observed [O III] $\lambda\lambda$ 4960,5008 doublets of these luminous quasars, broad components are more common than narrow core components ($\leqslant 1200$ km s^{-1}), and only one quasar shows stronger narrow components than broad. Two quasars exhibit significantly broad and blueshifted [O III] emission, thought to trace galactic-scale outflows, with median velocities of -610 and -1430 km s^{-1} relative to the [C II] 158 μm line. All eight quasars show strong optical Fe II emission and follow the eigenvector 1 relations defined by low-redshift quasars. The entire ASPIRE program will eventually cover 25 quasars and provide a statistical sample for the studies of the BHs and quasar spectral properties.

Unified Astronomy Thesaurus concepts: Quasars (1319); Supermassive black holes (1663); Reionization (1383)

1. Introduction

Observations of luminous $z \gtrsim 6.5$ quasars have revealed the existence of supermassive black holes (SMBHs) and their massive host galaxies in the reionization epoch. The measurements of high-redshift quasar BH masses suggest that 10^{8-9} solar-mass SMBHs existed as early as 700 million yr after the Big Bang, challenging models of early SMBH growth and BH seed formation (e.g., Bañados et al. 2018; Yang et al. 2020; Wang et al. 2021; Yang et al. 2021; Farina et al. 2022). Measuring BH masses accurately is the key step required to characterize the growth and evolution of early SMBHs. The way to obtain robust BH mass measurements is reverberation mapping (RM). However, this is not practically possible for $z > 4$ quasars. At higher redshift, the BH mass estimates are based on the so-called single-epoch virial BH mass using quasar broad emission lines.

The observations of quasar spectra in the rest-frame optical have been mostly confined to quasars at $z \lesssim 4$ (e.g., Shen 2016; Matthews et al. 2021) because of the difficulty in observing faint objects from the ground at wavelengths longer than the near-infrared K band. Thus, the measurements of SMBHs in quasars at $z > 4$ are mainly based on broad emission lines in the rest-frame UV (e.g., C IV λ1549 and Mg II λ2800). The Mg II-based BH mass estimators are widely used for the measurements of reionization-era SMBHs (e.g., Shen et al. 2019; Yang et al. 2021; Farina et al. 2022). However, the study of quasar BH masses at low redshift via RM and the comparison between multiple single-epoch BH mass estimators have established the Hβ line as the most reliable tracer among quasar UV/optical emission lines (e.g., Shen 2013; Wang et al. 2020). The existing Mg II-based scaling relation is indirectly calibrated based on the Hβ relation derived from RM, which introduces additional uncertainties. Therefore, high-sensitivity infrared (IR) spectroscopic observations covering the rest-frame optical emission are needed to better estimate the Hβ-based BH masses of quasars at the highest redshift.

A SPectroscopic survey of biased halos In the Reionization Era (ASPIRE) is a James Webb Space Telescope (JWST) Cycle 1 GO program that will observe a sample of 25 $z > 6.5$ quasars with JWST/NIRCam imaging and Wide Field Slitless Spectroscopy (WFSS; Wang et al. 2023). The WFSS observations will provide the spectra in the Hβ region for reionization-era quasars for the first time. In addition, the high-quality JWST spectra will allow us to study the spectral properties (e.g., continuum emission; [O III] $\lambda\lambda$ 4960, 5008; and optical Fe II emission) of quasars in the early universe. In this paper, we report JWST observations of eight ASPIRE quasars. They form the first sample of reionization-era quasars with spectral coverage in the rest-frame optical. We describe the observations and data reduction in Section 2. In Section 3, we report the main results from this early data, including the spectral fitting procedure, the Hβ-based BH masses, and the quasar optical emission-line properties. In Section 3, we also present detailed analysis of the blueshifted [O III] components and outflows observed in these quasars. We summarize our work in Section 4. All results assume a flat ΛCDM cosmology with parameters $\Omega_\Lambda = 0.7$, $\Omega_m = 0.3$, and $h = 0.7$.

2. Observations and Data Reduction

The eight quasar spectra used in this work are part of the medium-size JWST Cycle 1 program ASPIRE (PID 2078, PI: F. Wang; Wang et al. 2023), which carries out a spectroscopic survey in 25 reionization-era quasar fields using JWST/NIRCam WFSS using the F356W filter, as well as imaging observations in the F115W, F200W, and F356W bands at the same time. This program allows us to statistically investigate both reionization-era quasars and high-redshift galaxies in the quasar fields. The NIRCam spectral and imaging data set probes the rest-frame optical emission in a large sample of $z > 6.5$ quasars and host galaxies for the first time, which will improve our understanding of early SMBH activity and their host galaxies. The spectroscopic and imaging observations of the quasar fields allow studies of the environments of reionization-era quasars in a statistical manner, which will address the long-standing question of whether luminous quasars reside in the most massive dark matter halos and inhabit large-scale galaxy overdensities in the early universe.

The eight quasars reported in this work were observed with JWST/NIRCam in 2022 August and September. These targets were observed using the R-grism with F356W filter in long wavelength (LW) and F200W imaging in short wavelength (SW) simultaneously. We performed a three-point `INTRAMODULEX` primary dither with a `2-POINT-LARGE-WITH-NIRISS` subpixel dither. A `SHALLOW4` readout mode was used with nine groups per integration and one integration per exposure, which resulted in a total exposure time of 2834 s. After the grism observation, direct image and out-of-field images were taken in F356W (LW) and F115W (SW) with a total exposure time of 1417 s. For the analysis in this work, we only use the WFSS F356W spectral data of the quasar targets. Analysis of the spectra of galaxies in the quasar fields and

broadband imaging data will be presented in a set of subsequent papers.

The data reduction of imaging and WFSS data will be presented by Wang et al. (2023) in detail, and we will briefly describe the related steps below. The reduction of WFSS data used in this work was based on the JWST pipeline 1.7.2 and calibration reference data "jwst_0989.pmap." We started with `calwebb_detector1` to process the raw data and applied a custom step to `*_rate.fits` to remove the $1/f$ noise feature (Schlawin et al. 2020). We performed flat-fielding and assigned World Coordinate System for exposures and then generated master background models based on all existing ASPIRE observations. We constructed a tracing model and a dispersion model following the method used in Sun et al. (2022) and applied 2D spectral extraction to background-subtracted data. We used updated sensitivity functions based on Cycle 1 calibration programs (PID 1536, 1537, and 1538). Then the 1D spectra were extracted from individual exposures using optimal extraction (Horne 1986) and coadded with inverse variance weighting. The 1D spectra of the eight ASPIRE quasars are shown in Figure 1.

3. Rest-frame Optical Spectra of Reionization-era Quasars

In this section, we describe our spectral fitting procedure and the main results derived from this early sample. We measure the BH masses based on the Hβ line width and continuum luminosity and compare them with the measurements derived from their rest-frame UV spectra. We also discuss the profile of the [O III] emission lines and search for potential galactic-scale outflows. We note that the data reduction procedure of this new instrument is still in development, and the spectra might be slightly affected by future changes of the reduction pipeline, but the main findings in this paper will not be significantly affected. The final JWST ASPIRE data set will be presented after this program has been completed.

3.1. Spectra Fitting

We perform spectral fitting for each WFSS spectrum using a model consisting of continuum and emission lines. The redshift derived from the [C II] 158 μm line (Venemans et al. 2020; Yang et al. 2021; Wang et al. 2023) is used as the initial redshift. We use spectral data between observed wavelengths 31600 and 39500 Å, excluding edge regions where the calibration is less certain. This covers the rest-frame wavelength range of ∼4100–5200 Å for these quasars. We use a pseudocontinuum model including a power-law continuum and an empirical optical Fe II template from Boroson & Green (1992). To fit this pseudocontinuum, we choose continuum windows that are free of strong emission lines in quasar composite, [4150, 4230], [4435, 4700], and [5100, 5200] Å in the rest frame. For the two highest-redshift quasars, J0109–3047 and J0218+0007, we adjust the windows due to their limited spectral coverage on the red side. For the former, we only use the first two windows. For the latter, we extend the blue-side cutoff of the last window to 5060 Å.

Hβ and [O III] lines. We adopt the rest-frame vacuum wavelengths of 4862.68 Å for the Hβ line and 4960.30 Å and 5008.24 Å for the [O III] doublet (Vanden Berk et al. 2001). We employ a line model consisting of one narrow Gaussian component and three broad Gaussian components for the Hβ line (e.g., Shen 2016). For each [O III] line, we use one Gaussian for the narrow component (the "core" component) plus a second Gaussian profile for the potentially broadened and blueshifted component. For the object with strong blueshifted [O III] wings (i.e., J0224–4711), we include one more Gaussian for its broad [O III] component. We set a lower limit to the line FWHM of each component to be 200 km s^{-1}. This is based on the instrument resolution ($R \sim 1600$ at 4 μm). We also set an upper limit of 1200 km s^{-1} for all narrow components (e.g., Shen et al. 2011).

We tie the velocity shift and dispersion of the narrow Hβ to that of the [O III] "core" component. We assume a fixed line ratio of 3.0 between [O III] λ5008 Å and [O III] λ4960 Å for both "core" and broad components (e.g., Osterbrock & Ferland 2006). The velocity shifts of the broad [O III] components of each transition are also tied. We do not fix the line ratio between narrow Hβ component and narrow [O III] lines but limit the ratio of the "core" [O III] 5008 to the narrow Hβ to $\geqslant$1. If for an object, there is no narrow [O III] 5008 line, we consider that there should also be no narrow Hβ. For objects with narrow [O III] components, we derive [O III]-based redshifts using their narrow components and find that the [O III]-based redshifts show good agreement with their redshifts derived from [C II] 158 μm lines.

He II line. We test the possibility of including a He II line with a vacuum wavelength of 4687.02 Å by running alternate spectral decomposition. We include one Gaussian profile without constraining the line width and use a continuum window of [4435, 4635] Å instead of [4435, 4700] Å to avoid potential contamination from He II emission. We run the same spectral fitting procedure and fit the He II line together with the Hβ and [O III] lines. We find that only one quasar (J2232+2930) has an obvious He II line. Another quasar (J0218+0007) might have a narrow He II line, but it only has a significance of $\sim 2\sigma$. For these two, including He II reduces their BH masses by 4% and 2%, respectively. For other objects, their best-fit models do not show any need for a He II line, while the shorter continuum windows affect fits of their continuum, especially for $z > 6.7$ quasars. Thus, we finally only apply the He II fit for quasar J2232+2930, and for other quasars we keep the continuum window cutoff of 4700 Å. Even if there could be some weak He II emission in these quasars, their BH masses would not be affected significantly.

Hγ line. We also apply a two-Gaussian fit to the Hγ line at 4341.68 Å. The two Gaussian profiles are set for one narrow and one broad component. The same limits of narrow line width as used for Hβ are applied. The results are only used for plotting the best-fit but not any science analysis in this work.

We utilize a Monte Carlo (MC) approach to estimate the uncertainties of all spectral measurements, following Yang et al. (2021; also Shen et al. 2019; Wang et al. 2020). For each spectrum, we generate 50 mock spectra by randomly adding Gaussian noise at each pixel with a standard deviation equal to the spectral error at that pixel. We then perform the same spectral fitting procedure to each mock spectrum. The uncertainty of each spectral measurement is estimated by averaging the 16% and 84% percentile deviations from the median value. The best-fit results of all quasars are shown in Figure 1.

3.2. Hβ-based Black Hole Masses

The single-epoch virial method is widely used for estimating the BH mass of high-redshift quasars, assuming virial motion of the line-emitting gas in the quasar broad-line region (BLR) and

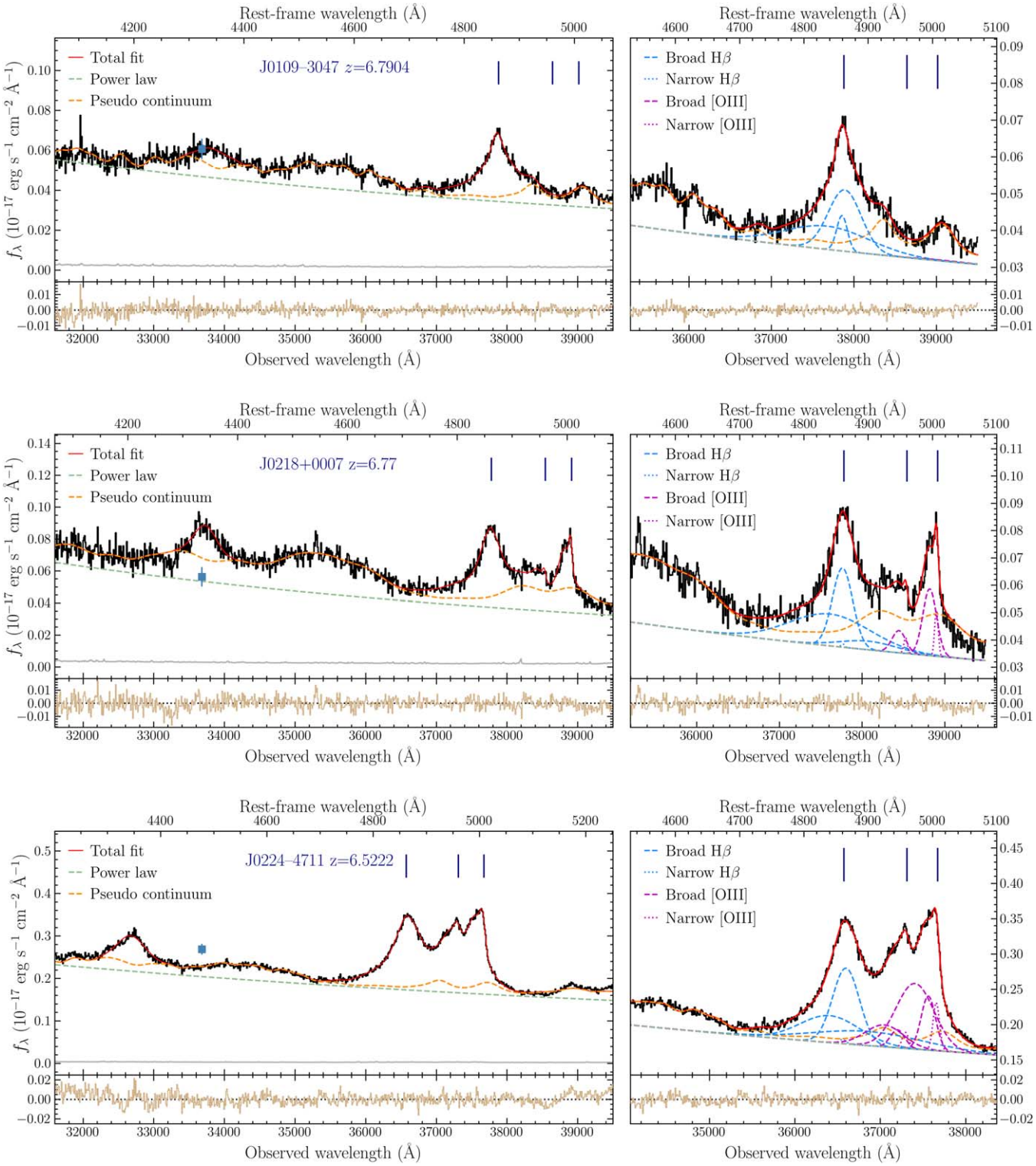

Figure 1. The JWST NIRCam WFSS F356W spectra of eight ASPIRE quasars (black line) with spectral uncertainty (gray), ordered by R.A. The red solid lines denote the best total fits. The best fits of different spectral components are shown with dashed and dotted lines. For each object, the left panel presents the entire spectrum with total fit, power-law continuum, and pseudocontinuum (i.e., power-law plus Fe II emission). The right panel shows the zoomed-in region of Hβ and [O III] lines. The systemic redshifts of the quasars are based on their [C II] line measurements from ALMA observations. The blue squares with error bars are the photometric data in the WISE W1 3.4 μm band. The panels below the spectra present the residuals (data model) of each best-fit model.

applying the empirical correlation between the BLR size and quasar continuum luminosity (i.e., the *R–L* relation). With this method, we can estimate the quasar central BH mass utilizing quasar broad emission lines and continuum luminosity. Quasar UV and optical emission lines, C IV λ1549 Å, Mg II λ2800 Å, Hα λ6563 Å, and Hβ have all been used as virial BH mass tracers (e.g., McLure & Jarvis 2002; Vestergaard 2002; McLure & Dunlop 2004; Onken et al. 2004; Greene & Ho 2005; Vestergaard & Peterson 2006; Vestergaard & Osmer 2009; Shen et al. 2011). Calibration coefficients used in these BH mass estimators are

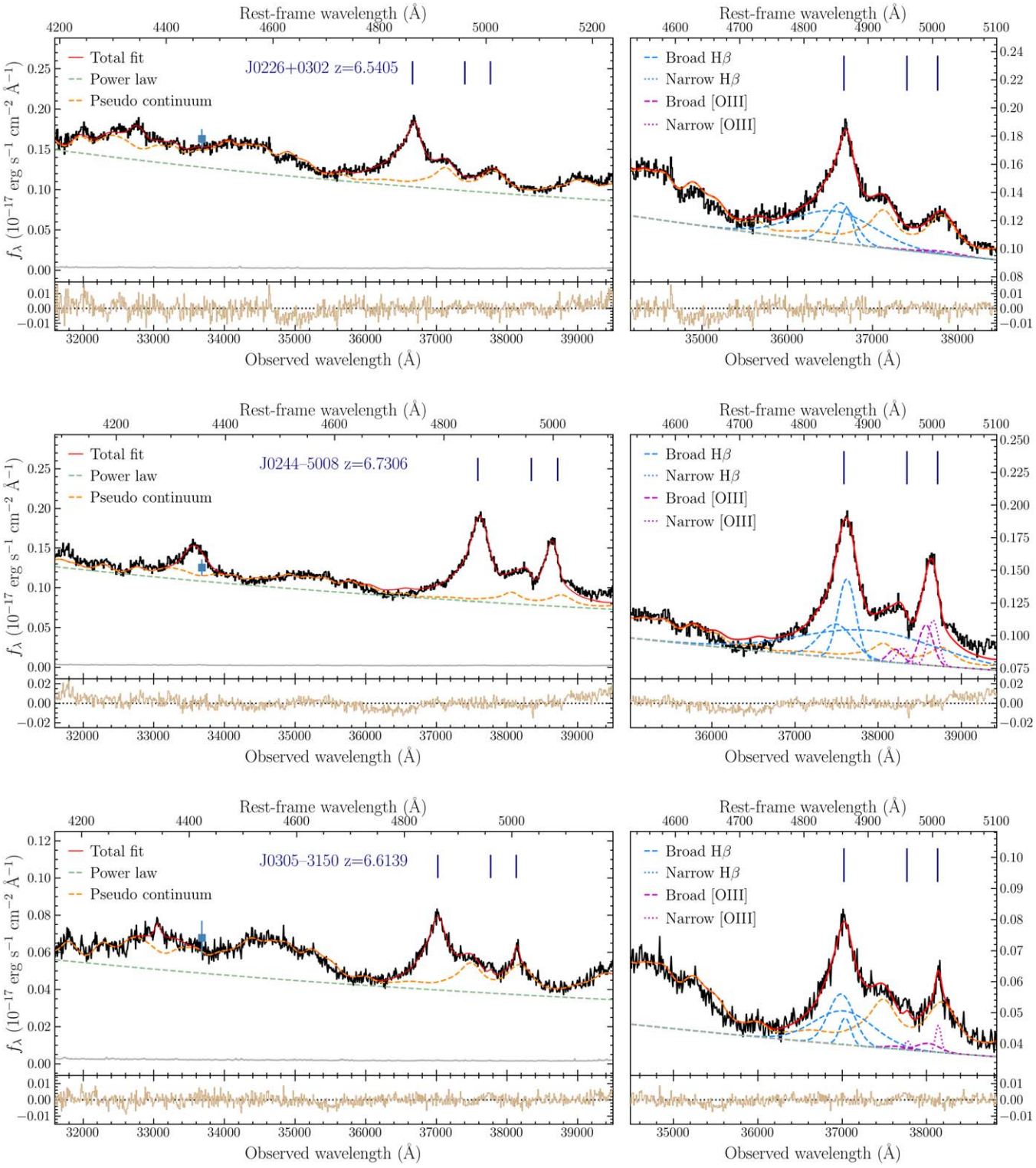

Figure 1. (Continued.)

determined using low-redshift quasar samples that have BH mass measurements based on RM. Among these lines, Hβ is often thought to be the most reliable tracer from both RM-based measurements and comparison of single-epoch mass estimators (e.g., Shen & Liu 2012).

We measure the single-epoch virial BH masses of these quasars based on their continuum luminosity at rest-frame 5100 Å and the Hβ line width, obtained from the spectral fitting. We adopt the BH mass estimator in Vestergaard & Peterson (2006),

$$\frac{M_{\rm BH,H\beta}}{M_\odot} = 10^{6.91}\left(\frac{\rm FWHM(H\beta)}{1000\ \rm km\ s^{-1}}\right)^2\left(\frac{\lambda L_\lambda(5100\ \text{Å})}{10^{44}\ \rm erg\ s^{-1}}\right)^{0.5}. \quad (1)$$

The 5100 Å continuum luminosity is derived from the best-fit power-law continuum directly. The systematic scatter of this

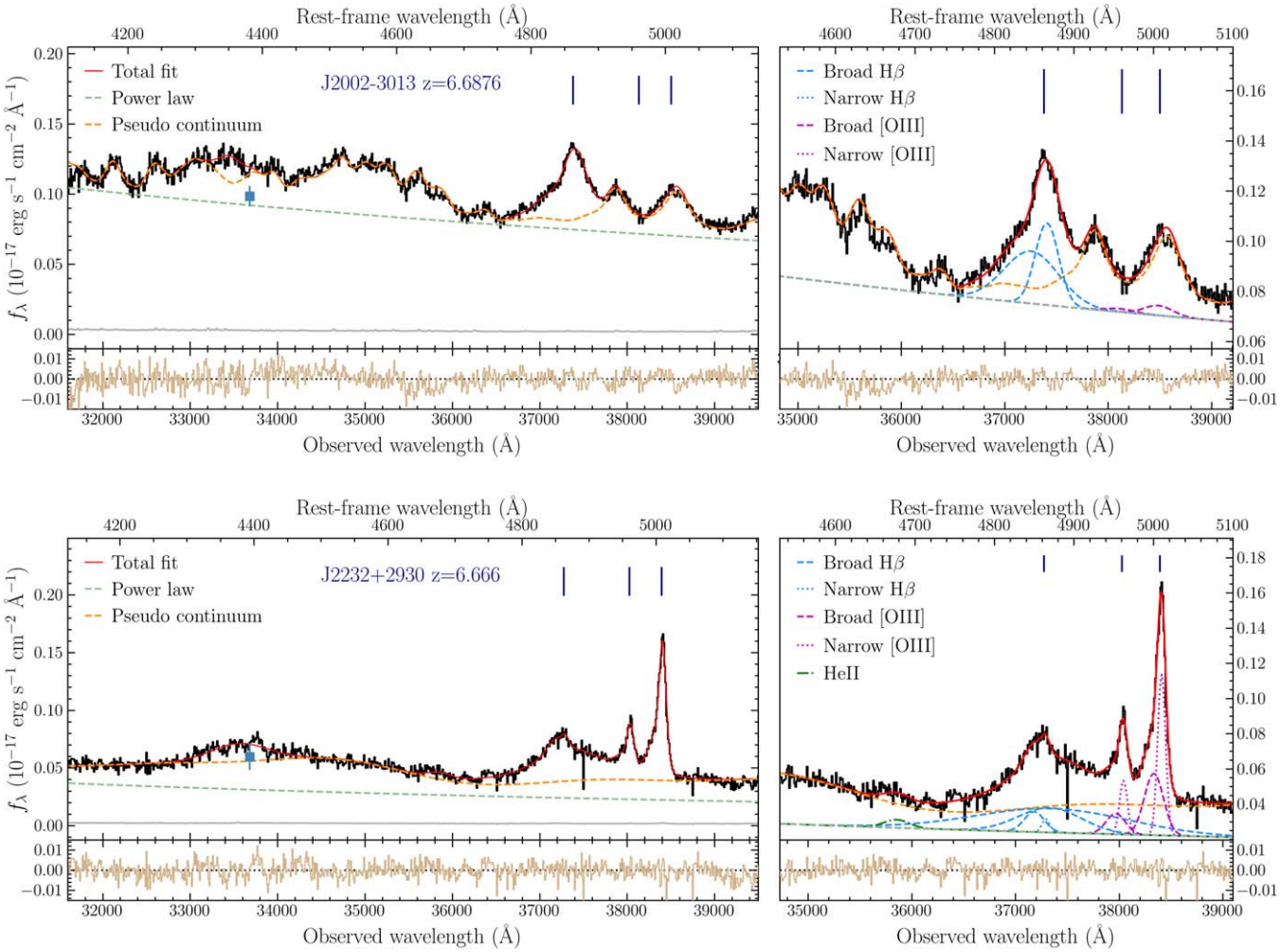

Figure 1. (Continued.)

BH mass estimator relative to RM mass is ∼0.4–0.5 dex, which is not included when we report the errors of BH mass measurements. The uncertainties of all measurements are derived from the MC approach, as described above. We then compute the Eddington ratio ($\lambda_{\rm Edd} = L_{\rm bol}/L_{\rm Edd}$) for each quasar. The bolometric luminosity is estimated by multiplying the 5100 Å luminosity by 9.26 (Richards et al. 2006). Table 1 summarizes the redshift, Hβ line width, continuum luminosity, Hβ BH mass, Eddington ratio, and Mg II BH mass of each of the eight quasars.

The Hβ-based measurements show that these quasars have BH masses in the range of (0.6–2.1) $\times 10^9\,M_\odot$. These quasars all have been published with measurements of BH mass based on the Mg II emission lines from their near-infrared (NIR) spectroscopic data (e.g., Mazzucchelli et al. 2017; Reed et al. 2019; Schindler et al. 2020; Wang et al. 2021; Yang et al. 2021; Farina et al. 2022). We adopt the most recent measurements of these eight quasars from Reed et al. (2019), Wang et al. (2021), Yang et al. (2021), and Farina et al. (2022). All of these Mg II-based BH masses are computed using the BH mass estimator from Vestergaard & Osmer (2009). Figure 2 shows the Hβ-based BH masses compared to their Mg II-based BH masses. The BH masses derived from the Hβ lines and 5100 Å luminosity are consistent with the Mg II-based measurements within their systematic scatters (i.e., ∼0.4–0.5 dex). Recently, a new measurement of BH mass of quasar J0100+2802 at $z = 6.3$ using the Hβ line from JWST observations also shows agreement with its Mg II-based BH mass within systematic uncertainties (Eilers et al. 2022).

In our quasar sample, the differences between these two BH mass estimates span from −0.32 to 0.22 dex, comparable to the scatter shown in the SDSS low-redshift quasar sample (a standard deviation of ∼0.38 dex; Shen et al. 2011). Among these eight quasars, there is a trend that the Hβ-based BH masses are slightly smaller, with an average $M_{\rm BH,H\beta}$–$M_{\rm BH,Mg\,II}$ of −0.13 dex. However, the current sample is too small to conclude if there is a systematic offset. The Hβ-based BH masses and the comparison between Hβ and Mg II measurements confirm the existence of a billion solar-mass BHs in the reionization epoch. These SMBHs require $\gtrsim 10^{2-3}\,M_\odot$ seed BHs at $z = 30$ assuming Eddington accretion across the entire time since BH seeding and a radiative efficiency of 0.1 (e.g., Yang et al. 2021; Farina et al. 2022). This thus raises the questions of how to maintain highly accreting BHs for the long term and how to form massive seed BHs in the early universe (e.g., Volonteri 2012; Davies et al. 2019; Inayoshi et al. 2020).

These measurements are derived from the spectral fits of the NIR spectra and JWST spectra separately. Thus, for both data sets, the limited continuum windows might lead to additional

Table 1
Spectral Fitting and Quasar Properties

Name	$z_{[\mathrm{C\ II}]}$	$z_{[\mathrm{O\ III}]}$[a]	$M_{\mathrm{BH,H}\beta}$ ($10^9\,M_\odot$)	$\mathrm{FWHM}_{\mathrm{H}\beta}$ (km s^{-1})	L_{5100} (10^{45}erg s^{-1})	λ_{Edd}	$M_{\mathrm{BH,Mg\ II}}$ ($10^9\,M_\odot$)	Ref_Mg II[b]
J010953.13–304726.30	6.7904 ± 0.0003	⋯	0.60 ± 0.05	3033.0 ± 117.0	6.40 ± 0.08	0.76 ± 0.06	$1.11^{+0.4}_{-0.36}$	Farina+2022
J021847.04+000715.20	6.7700 ± 0.0013	6.7668 ± 0.0006	0.61 ± 0.05	3030.0 ± 117.0	6.71 ± 0.16	0.78 ± 0.07	0.61 ± 0.07	Yang+2021
J022426.54–471129.40	6.5222 ± 0.0001	6.5186 ± 0.0004	2.15 ± 0.09	3936.0 ± 78.0	29.19 ± 0.09	0.97 ± 0.04	1.30 ± 0.18	Wang+2021
J022601.87+030259.28	6.5405 ± 0.0001	⋯	1.05 ± 0.09	3131.0 ± 129.0	17.25 ± 0.09	1.17 ± 0.09	2.20 ± 0.39	Wang+2021
J024401.02–500853.70	6.7306 ± 0.0002	6.720 ± 0.003	0.88 ± 0.10	2969.0 ± 158.0	15.08 ± 0.13	1.22 ± 0.12	1.15 ± 0.39	Reed+2019
J030516.92–315056.00	6.6139 ± 0.0002	6.615 ± 0.001	0.62 ± 0.14	3020.0 ± 314.0	6.95 ± 0.06	0.80 ± 0.14	0.70 ± 0.38	Wang+2021
J200241.59–301321.69	6.6876 ± 0.0004	⋯	0.84 ± 0.04	2981.0 ± 79.0	13.65 ± 0.10	1.15 ± 0.06	1.62 ± 0.27	Yang+2021
J223255.15+293032.04	6.666 ± 0.004	6.669 ± 0.0001	1.93 ± 0.13	6044.0 ± 201.0	4.24 ± 0.10	0.16 ± 0.01	3.06 ± 0.36	Yang+2021

Notes.
[a] The [O III] redshift is estimated based on the line center of the "core" component of [O III] 5008 line. Quasars J0109–3047, J0226+0302, and J2002–3013 do not have narrow [O III] components, and thus we do not estimate their [O III] redshift.
[b] The references of the Mg II-based BH masses adopted in this work.

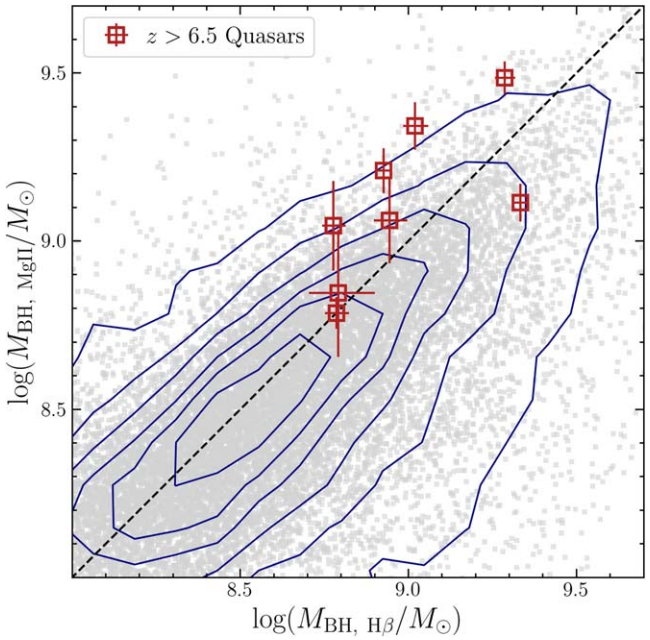

Figure 2. The BH masses of eight ASPIRE quasars (red squares), measured from the Hβ lines in JWST/NIRCam WFSS spectra and the Mg II lines in their NIR spectra. These are compared with the measurements of low-z quasars from the SDSS Data Release 7 (DR7) sample (Shen et al. 2011) using the same Mg II and Hβ BH mass estimators (gray small squares and blue contours). The differences between $M_{\rm BH,H\beta}$ and $M_{\rm BH,Mg\ II}$ of these high-redshift quasars are comparable to the scatter shown in the low-redshift quasar sample. The mean value of $M_{\rm BH,H\beta}$–$M_{\rm BH,Mg\ II}$ is −0.13 dex, while the sample size is too small to identify a systematic offset.

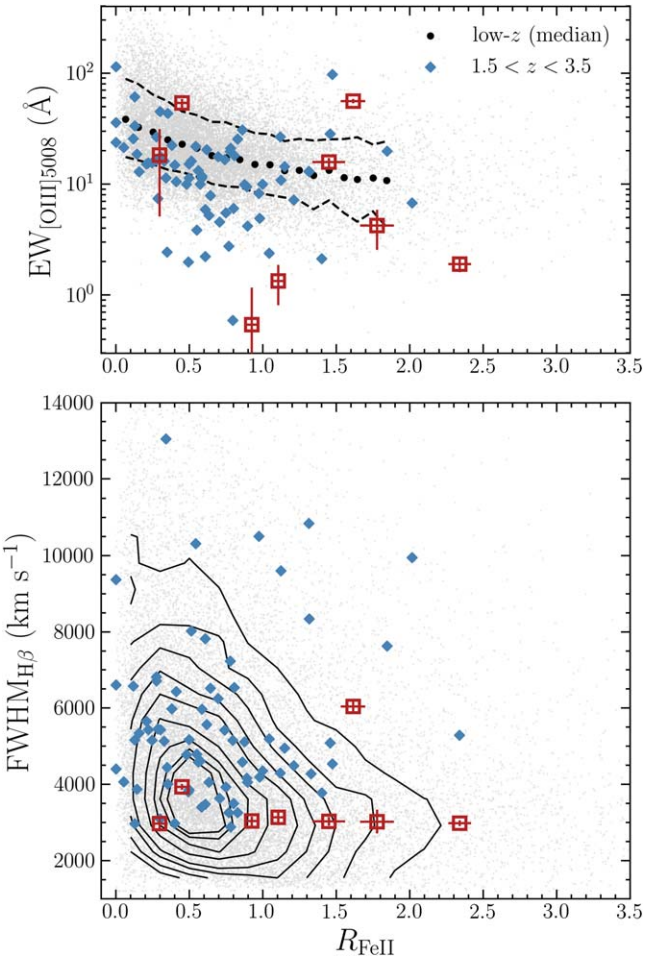

Figure 3. EV1 relations using our eight high-redshift quasars (red squares), compared with luminous quasars at intermediate redshift (Shen 2016; open diamonds) and SDSS low-z quasars (Shen et al. 2011; gray dots). The black filled circles and the dashed lines denote the median, 16th, and 84th percentiles of the SDSS low-z quasars at each redshift bin. These reionization-era quasars generally follow the trends observed in lower-redshift quasars.

uncertainties of the spectral decomposition and BH mass measurements. In the next step, we will utilize the entire ASPIRE sample to perform a detailed comparison between the Hβ and Mg II BH masses when observations of the full sample are complete. With the final sample, we will combine the NIR and JWST spectra as well as the JWST F115W, F200W, and F356W photometries and will apply joint spectral analysis. The combined data set will provide a wider continuum window and allow a better separation of the Fe II emission from the featureless continuum.

3.3. Optical Spectral Properties and [O III] Outflows

The most important spectral quantities covered by the WFSS spectra are the Hβ, [O III], and Fe II emission. In general, all eight quasars have strong and broad Hβ lines, with FWHM ranging from 3000 to 6000 km s^{-1}. Optical Fe II emission is clearly seen in all eight quasars. The observed [O III] doublets in these quasars have relatively diverse properties. Three of these quasars, J0109–3047, J0226+0302, and J2002–3013, show similar profiles in their [O III] line regions, with very weak broad-only [O III] doublets but no narrow [O III] lines (i.e., the "core" component, $<$1200 km s^{-1}). The other five quasars all have both narrow and broad [O III] components. Quasar J2232+2930 has the strongest narrow [O III] lines among these quasars. It is the only object observed with stronger narrow [O III] lines relative to its broad components.

Using the WFSS data, we are able to visit the eigenvector 1 (EV1) relations (Boroson & Green 1992) in the most distant quasars. The EV1 relations describe the relationships between emission-line quantities and the strength of the optical Fe II emission and has been widely investigated in the past three decades with quasar samples at $z < 4$ (e.g., Boroson & Green 1992; Marziani et al. 2001; Boroson 2002; Shen & Ho 2014). The anticorrelation between the strength of [O III] and Fe II emission is one of the most important EV1 relations observed. The trend of Fe II strength, as the Hβ FWHM decreases, is also a probe of the physical drivers of the EV1 relations. We study the correlation of the [O III] 5008 EW and $\rm FWHM_{H\beta}$ with the $R_{\rm Fe\ II}$ (Shen 2016) and compare them with the observations of the luminous intermediate-redshift ($1.5 < z < 3.5$) sample in Shen (2016) and the low-redshift ($z < 1$) quasars from the SDSS DR7 (Shen et al. 2011). The $\rm EW_{[O\ III]5008}$ used here is the EW of the entire [O III] λ5008 line in order to compare our results with the measurements from Shen (2016). $\rm FWHM_{H\beta}$ is the line width of the broad Hβ. $R_{\rm Fe\ II}$ is the ratio of $\rm EW_{Fe\ II}$ and $\rm EW_{H\beta}$, and the Fe II EW is measured between 4434 and 4684 Å.

As shown in Figure 3, overall, the optical spectral quantities in these high-redshift quasars follow the relations defined in lower-redshift quasars. Our high-redshift quasars show slightly lower [O III] EW than the mean values of SDSS low-redshift quasars and are more similar to the luminous $1.5 < z < 3.5$ quasar sample, which is due to their high luminosity and the Baldwin effect (Baldwin 1977). There is no significant outlier

among our high-redshift quasars. The three lowest [O III] EWs are from the quasars with weak and broad-only [O III] emission. In the $\mathrm{FWHM}_{\mathrm{H}\beta}$ versus $R_{\mathrm{Fe\,II}}$ plane, our objects distribute in a narrow $\mathrm{FWHM}_{\mathrm{H}\beta}$ range with lower $\mathrm{FWHM}_{\mathrm{H}\beta}$ than the intermediate-redshift sample. This is consistent with the high Eddington ratios of most (7 of 8) of our high-z quasars. The general consistency between our sample and low-z distributions suggests that the EV1 relations might exist in quasars as early as the reionization epoch, and our full ASPIRE sample will enable more detailed comparisons with low-z samples.

Broad, skewed, and blue/redshifted [O III] profiles have been discovered in quasars at $z \lesssim 3.5$ and used to probe kiloparsec-scale outflows in quasar host galaxies (e.g., Cano-Díaz et al. 2012; Carniani et al. 2015; Zakamska et al. 2016; Bischetti et al. 2017). At $z > 6$, outflows powered by the central active galactic nucleus are a common prediction of a broad range of cosmological simulations (e.g., Dubois et al. 2013; Costa et al. 2014, 2022; Lupi et al. 2022). However, observational evidence of large-scale outflows in quasar hosts remains anecdotal at this redshift. The JWST data set provides us with the first chance to search for [O III] outflows in reionization-era quasars. Two quasars, J0218+0007 and J0224–4711, have prominently strong broad and blueshifted [O III] components, with a velocity shift of $-630\,\mathrm{km\,s^{-1}}$ and $-1690\,\mathrm{km\,s^{-1}}$ relative to the narrow [O III], respectively. Figure 4 shows their zoomed-in [O III] λ5008 lines, with other components subtracted out according to the best-fit models. We compute the median velocity, v_{50}, the velocity at the 50th percentile of the line flux; v_{10} and v_{90}, the velocities at the 10th and 90th percentiles; and w_{80} ($=v_{90} - v_{10}$), containing 80% of the total line power, which is close to the commonly used FWHM ($w_{80} = 1.088$ FWHM) for a Gaussian profile. The velocities are calculated relative to their [C II] redshifts. J0218+0007 has a median velocity (v_{50}) of $\sim -610\,\mathrm{km\,s^{-1}}$, with a v_{90} of $-1510\,\mathrm{km\,s^{-1}}$ and a w_{80} of $1590\,\mathrm{km\,s^{-1}}$. J0224–4711 has a median velocity (v_{50}) of $\sim -1430\,\mathrm{km\,s^{-1}}$, a v_{90} of $-4010\,\mathrm{km\,s^{-1}}$, and a w_{80} of $\sim 4140\,\mathrm{km\,s^{-1}}$.

Their broad [O III] widths and high-velocity shifts make them stand out among the quasar population. Particularly, J0224–4711 has one of the most extreme broad and blueshifted [O III] lines observed to date, even compared to the observations of lower-redshift quasars. For example, the $1.5 < z < 3.5$ luminous quasars in Shen (2016) have a median [O III] FWHM of $900\,\mathrm{km\,s^{-1}}$, with the broadest one to $2100\,\mathrm{km\,s^{-1}}$. Zakamska et al. (2016) observed extreme outflows in red luminous quasars at $z \sim 2$–3 and discovered broad [O III] with w_{80} ranging between 3600 and $5500\,\mathrm{km\,s^{-1}}$, strongly blueshifted up to $1500\,\mathrm{km\,s^{-1}}$. The more recent study of hyperluminous quasars at $z \sim 2$–4 revealed a population of [O III] lines with FWHM of 1200–2200 $\mathrm{km\,s^{-1}}$ (Bischetti et al. 2017). Large velocity widths and high velocities of blueshifted [O III] suggest powerful ionized outflows, while the nature of high-velocity large-scale gas in quasars is still debated. The most blueshifted [O III] lines observed in the extremely red $z = 2$–3 quasars are thought to be caught during a "blow-out" phase of quasar evolution and associated with fast ionized outflows (e.g., Zakamska et al. 2016; Perrotta et al. 2019; Vayner et al. 2021). So far, there is no evidence of J0218+0007 and J0224–4711 being extremely red quasars. A detailed multiwavelength analysis will be conducted in the future to better understand the physical properties of their fast outflows. In addition, a joint analysis of the 1D spectra and 2D images will be performed in subsequent works to examine the host galaxies and outflows. In the next step, JWST NIRSpec/IFU follow-up observations will be carried out to reveal the nature of their outflows. The entire ASPIRE sample will allow us to systematically study [O III] outflows in the reionization-era quasars, in synergy with multiwavelength imaging and spectroscopic data.

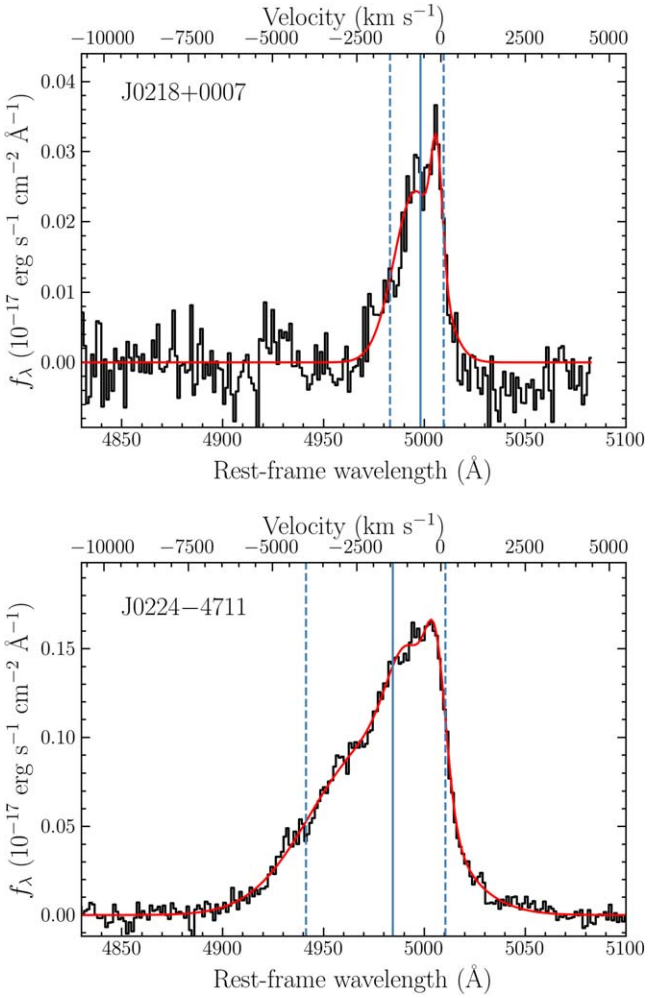

Figure 4. The [O III] 5008 lines with strong broad and blueshifted components have been observed in two quasars, J0218+0007 (top) and J0224–4711 (bottom). The blue solid lines denote the median velocity (v_{50}), and the dashed lines mark the part containing 80% of the line power (w_{80}). J0218+0007 has a v_{50} of $\sim -610\,\mathrm{km\,s^{-1}}$ and a w_{80} of $1590\,\mathrm{km\,s^{-1}}$; quasar J0224–4711 has a more remarkable [O III], with a v_{50} of $\sim -1430\,\mathrm{km\,s^{-1}}$ and a w_{80} of $4140\,\mathrm{km\,s^{-1}}$. These blueshifted broad lines, in particular in J0224–4711, are comparable to the most extreme cases observed at lower redshift (e.g., Zakamska et al. 2016; Bischetti et al. 2017).

4. Summary

In this paper, we present the results from an early sample of ASPIRE JWST/WFSS spectral data set consisting of eight quasars at $z > 6.5$, observed in 2022 August and September. With these high-quality WFSS spectra, we are able to study the rest-frame optical emission in reionization-era quasars for the first time. We measure the virial BH masses using the Hβ lines and compare them with the Mg II-based measurements. We find that, in general, the Hβ BH masses are consistent with the Mg II BH masses within the systematic uncertainties of the BH mass estimators. The discrepancy is within the scatter between

these two measurements as gauged from lower-redshift quasar samples. Therefore, using a more reliable tracer, the Hβ line, we confirm the existence of a billion solar-mass BHs in the reionization epoch.

We also test the optical spectral properties of these reionization-era quasars in the EV1 plane defined by $z < 4$ quasars. The results suggest that EV1 relations exist in these distant quasars and our quasars are distributed similarly to the luminous quasars at intermediate redshift. We discover two quasars with broad and strongly blueshifted [O III] lines. One of them has a prominent broad [O III] profile ($w_{80} = 4140\ \mathrm{km\ s^{-1}}$) with a high-velocity shift ($v_{50} = -1430\ \mathrm{km\ s^{-1}}$), which is among the most extreme cases, even compared to observations in lower-redshift quasars.

With the ASPIRE program, we will construct a sample of 25 quasars with not only JWST WFSS spectra and NIRCam images but also the data from multiwavelength observations, spanning X-ray to submillimeter and radio. The final sample will be used for detailed investigations of their BH physics, quasar feedback, and host galaxy properties.

Acknowledgments

J.Y. and X.F. acknowledge support from US NSF grants AST 19-08284. F.W. acknowledges support by NASA through the NASA Hubble Fellowship grant #HST-HF2-51448.001-A awarded by the Space Telescope Science Institute, which is operated by the Association of Universities for Research in Astronomy, Incorporated, under NASA contract NAS5-26555. Research at UC Irvine was supported by NSF grant AST-1907290. F.S. and E.E. acknowledge funding from JWST/NIRCam contract to the University of Arizona, NAS5-02105. J.T.S. acknowledges funding from the European Research Council (ERC) Advanced Grant program under the European Union's Horizon 2020 research and innovation program (grant agreement No. 885301). L.B. acknowledges support from NSF award AST-1909933 and NASA award #80NSSC22K0808. S. E.I.B. acknowledges funding from the European Research Council (ERC) under the European Union's Horizon 2020 research and innovation program (grant agreement No. 740246 "Cosmic Gas." M.H. acknowledges support from the Zentrum für Astronomie der Universität Heidelberg under the Gliese Fellowship. Z.H. acknowledges support from NSF grant AST-2006176. G.K. is partly supported by the Department of Atomic Energy (Government of India) research project with Project Identification Number RTI 4002, and by the Max Planck Society through a Max Planck Partner Group. A.L. acknowledges funding from MIUR under the grant PRIN 2017-MB8AEZ. S.R.R. acknowledges financial support from the International Max Planck Research School for Astronomy and Cosmic Physics at the University of Heidelberg (IMPRS-HD). B.T. acknowledges support from the European Research Council (ERC) under the European Union's Horizon 2020 research and innovation program (grant agreement 950533) and from the Israel Science Foundation (grant 1849/19). M.T. acknowledges support from the NWO grant 0.16.VIDI.189.162 ("ODIN"). M.V. gratefully acknowledges support from the Independent Research Fund Denmark via grant No. DFF 8021-00130.

This work is based on observations made with the NASA/ESA/CSA James Webb Space Telescope. These observations are associated with program #2078. Support for program #2078 was provided by NASA through a grant from the Space Telescope Science Institute, which is operated by the Association of Universities for Research in Astronomy, Inc., under NASA contract NAS5-03127. All of the data presented in this paper were obtained from the Mikulski Archive for Space Telescopes (MAST) at the Space Telescope Science Institute. The specific observations analyzed can be accessed.[42]

Facility: JWST(NIRCam).

Software: astropy (Astropy Collaboration et al. 2018), Matplotlib (Hunter 2007), Numpy (Harris et al. 2020), Photutils (Bradley et al. 2022), Scipy (Virtanen et al. 2020).

ORCID iDs

Jinyi Yang https://orcid.org/0000-0001-5287-4242
Feige Wang https://orcid.org/0000-0002-7633-431X
Xiaohui Fan https://orcid.org/0000-0003-3310-0131
Joseph F. Hennawi https://orcid.org/0000-0002-7054-4332
Aaron J. Barth https://orcid.org/0000-0002-3026-0562
Eduardo Bañados https://orcid.org/0000-0002-2931-7824
Fengwu Sun https://orcid.org/0000-0002-4622-6617
Weizhe Liu https://orcid.org/0000-0003-3762-7344
Zheng Cai https://orcid.org/0000-0001-8467-6478
Linhua Jiang https://orcid.org/0000-0003-4176-6486
Zihao Li https://orcid.org/0000-0001-5951-459X
Masafusa Onoue https://orcid.org/0000-0003-2984-6803
Jan-Torge Schindler https://orcid.org/0000-0002-4544-8242
Yue Shen https://orcid.org/0000-0003-1659-7035
Yunjing Wu https://orcid.org/0000-0003-0111-8249
Aklant K. Bhowmick https://orcid.org/0000-0002-7080-2864
Laura Blecha https://orcid.org/0000-0002-2183-1087
Sarah Bosman https://orcid.org/0000-0001-8582-7012
Jaclyn B. Champagne https://orcid.org/0000-0002-6184-9097
Thomas Connor https://orcid.org/0000-0002-7898-7664
Tiago Costa https://orcid.org/0000-0002-6748-2900
Frederick B. Davies https://orcid.org/0000-0003-0821-3644
Roberto Decarli https://orcid.org/0000-0002-2662-8803
Gisella De Rosa https://orcid.org/0000-0003-3242-7052
Alyssa B. Drake https://orcid.org/0000-0002-0174-3362
Eiichi Egami https://orcid.org/0000-0003-1344-9475
Anna-Christina Eilers https://orcid.org/0000-0003-2895-6218
Analis E. Evans https://orcid.org/0000-0003-0850-7749
Emanuele Paolo Farina https://orcid.org/0000-0002-6822-2254
Zoltan Haiman https://orcid.org/0000-0003-3633-5403
Xiangyu Jin https://orcid.org/0000-0002-5768-738X
Hyunsung D. Jun https://orcid.org/0000-0003-1470-5901
Koki Kakiichi https://orcid.org/0000-0001-6874-1321
Yana Khusanova https://orcid.org/0000-0002-7220-397X
Girish Kulkarni https://orcid.org/0000-0001-5829-4716
Alessandro Lupi https://orcid.org/0000-0001-6106-7821
Chiara Mazzucchelli https://orcid.org/0000-0002-5941-5214
Zhiwei Pan https://orcid.org/0000-0003-0230-6436
Sofía Rojas-Ruiz https://orcid.org/0000-0003-2349-9310
Michael A. Strauss https://orcid.org/0000-0002-0106-7755
Wei Leong Tee https://orcid.org/0000-0003-0747-1780

[42] doi:10.17909/vt74-kd84

Benny Trakhtenbrot https://orcid.org/0000-0002-3683-7297
Maxime Trebitsch https://orcid.org/0000-0002-6849-5375
Bram Venemans https://orcid.org/0000-0001-9024-8322
Marianne Vestergaard https://orcid.org/0000-0001-9191-9837
Marta Volonteri https://orcid.org/0000-0002-3216-1322
Fabian Walter https://orcid.org/0000-0003-4793-7880
Zhang-Liang Xie https://orcid.org/0000-0002-0125-6679
Minghao Yue https://orcid.org/0000-0002-5367-8021
Haowen Zhang https://orcid.org/0000-0002-4321-3538
Huanian Zhang https://orcid.org/0000-0002-0123-9246
Siwei Zou https://orcid.org/0000-0002-3983-6484

References

Astropy Collaboration, Price-Whelan, A. M., Sipőcz, B. M., et al. 2018, AJ, 156, 123
Baldwin, J. A. 1977, ApJ, 214, 679
Bañados, E., Venemans, B. P., Mazzucchelli, C., et al. 2018, Natur, 553, 473
Bischetti, M., Piconcelli, E., Vietri, G., et al. 2017, A&A, 598, A122
Boroson, T. A. 2002, ApJ, 565, 78
Boroson, T. A., & Green, R. F. 1992, ApJS, 80, 109
Bradley, L., Sipőcz, B., Robitaille, T., et al. 2022, astropy/photutils: v1.5.0, Zenodo, doi:10.5281/zenodo.6825092
Cano-Díaz, M., Maiolino, R., Marconi, A., et al. 2012, A&A, 537, L8
Carniani, S., Marconi, A., Maiolino, R., et al. 2015, A&A, 580, A102
Costa, T., Arrigoni Battaia, F., Farina, E. P., et al. 2022, MNRAS, 517, 1767
Costa, T., Sijacki, D., Trenti, M., et al. 2014, MNRAS, 439, 2146
Davies, F. B., Hennawi, J. F., & Eilers, A.-C. 2019, ApJL, 884, L19
Dubois, Y., Pichon, C., Devriendt, J., et al. 2013, MNRAS, 428, 2885
Eilers, A.-C., Simcoe, R. A., Yue, M., et al. 2022, arXiv:2211.16261
Farina, E. P., Schindler, J.-T., Walter, F., et al. 2022, ApJ, 941, 106
Greene, J. E., & Ho, L. C. 2005, ApJ, 630, 122
Harris, C. R., Millman, K. J., van der Walt, S. J., et al. 2020, Natur, 585, 357
Horne, K. 1986, PASP, 98, 609
Hunter, J. D. 2007, CSE, 10, 1109
Inayoshi, K., Visbal, E., & Haiman, Z. 2020, ARA&A, 58, 27
Lupi, A., Volonteri, M., Decarli, R., et al. 2022, MNRAS, 510, 5760
Marziani, P., Sulentic, J. W., Zwitter, T., et al. 2001, ApJ, 558, 553
Matthews, B. M., Shemmer, O., Dix, C., et al. 2021, ApJS, 252, 15
Mazzucchelli, C., Bañados, E., Venemans, B. P., et al. 2017, ApJ, 849, 91
McLure, R. J., & Dunlop, J. S. 2004, MNRAS, 352, 1390
McLure, R. J., & Jarvis, M. J. 2002, MNRAS, 337, 109
Onken, C. A., Ferrarese, L., Merritt, D., et al. 2004, ApJ, 615, 645
Osterbrock, D. E., & Ferland, G. J. (ed.) 2006, Astrophysics of Gaseous Nebulae and Active Galactic Nuclei (2nd ed.; Sausalito, CA: Univ. Science Books)
Perrotta, S., Hamann, F., Zakamska, N. L., et al. 2019, MNRAS, 488, 4126
Reed, S. L., Banerji, M., Becker, G. D., et al. 2019, MNRAS, 487, 1874
Richards, G. T., Lacy, M., Storrie-Lombardi, L. J., et al. 2006, ApJS, 166, 470
Schindler, J.-T., Farina, E. P., Bañados, E., et al. 2020, ApJ, 905, 51
Schlawin, E., Leisenring, J., Misselt, K., et al. 2020, AJ, 160, 231
Shen, Y. 2013, BASI, 41, 61
Shen, Y. 2016, ApJ, 817, 55
Shen, Y., & Ho, L. C. 2014, Natur, 513, 210
Shen, Y., & Liu, X. 2012, ApJ, 753, 125
Shen, Y., Richards, G. T., Strauss, M. A., et al. 2011, ApJS, 194, 45
Shen, Y., Wu, J., Jiang, L., et al. 2019, ApJ, 873, 35
Sun, F., Egami, E., Pirzkal, N., et al. 2022, arXiv:2209.03374
Vanden Berk, D. E., Richards, G. T., Bauer, A., et al. 2001, AJ, 122, 549
Vayner, A., Zakamska, N. L., Riffel, R. A., et al. 2021, MNRAS, 504, 4445
Venemans, B. P., Walter, F., Neeleman, M., et al. 2020, ApJ, 904, 130
Vestergaard, M. 2002, ApJ, 571, 733
Vestergaard, M., & Osmer, P. S. 2009, ApJ, 699, 800
Vestergaard, M., & Peterson, B. M. 2006, ApJ, 641, 689
Virtanen, P., Gommers, R., Oliphant, T. E., et al. 2020, NatMe, 17, 261
Volonteri, M. 2012, Sci, 337, 544
Wang, F., Fan, X., Yang, J., et al. 2021, ApJ, 908, 53
Wang, S., Shen, Y., Jiang, L., et al. 2020, ApJ, 903, 51
Wang, F., Yang, J., Hennawi, J.-F., et al. 2023, arXiv:2304.09894
Yang, J., Wang, F., Fan, X., et al. 2020, ApJL, 897, L14
Yang, J., Wang, F., Fan, X., et al. 2021, ApJ, 923, 262
Zakamska, N. L., Hamann, F., Pâris, I., et al. 2016, MNRAS, 459, 3144